Biosurface and Biotribology

WILEY

The Institution of Engineering and Technology

ORIGINAL RESEARCH OPEN ACCESS

Investigation of the Long-Term Degradation Behaviour of Binary Mesoporous Bioactive Glass Nanoparticles

Jing Tian[1] | Meng Luo[2] | Mi Chen[3] | Yanzi Zhao[1] | Bo Lei[1]

[1]Frontier Institute of Science and Technology, Xi'an Jiaotong University, Xi'an, China | [2]School of Life Science and Technology, Xidian University, Xi'an, China | [3]Shaanxi Key Laboratory of Biomedical Metallic Materials, Northwest Institute for Non-Ferrous Metal Research, Xi'an, China

Correspondence: Bo Lei (rayboo@xjtu.edu.cn)

Received: 30 December 2025 | **Revised:** 3 May 2026 | **Accepted:** 9 May 2026

Keywords: bioactive glass | ion degradation and release | metal ion doping | silicate network structure

ABSTRACT

Bioactive glass nanoparticles (BGNs) have attracted widespread attention in regenerative medicine owing to their excellent biocompatibility and tissue repair capacity. However, the ion release behaviour associated with the long-term degradation of BGNs doped with different functional elements remains unclear. Herein, binary silicate BGNs (BGN-Ca, BGN-Mg, BGN-Zn, BGN-Cu and BGN-Mn) were prepared, and their degradation behaviour in normal saline was systematically evaluated over a period of up to 150 days. The evolution of particle morphology and size, ion release and pH changes in solution was characterised in detail. The results showed that the degradation behaviours of BGNs doped with different elements differed markedly. BGN-Ca and BGN-Mg exhibited the fastest degradation rates characterised by rapid degradation accompanied by higher Si release, whereas BGN-Zn and BGN-Mn showed comparable total Si release but displayed 'fast-then-slow' and 'slow-then-fast' release patterns, respectively. Overall, the reactivity of metal ions can provide a preliminary prediction of early ion-exchange trends, but the actual degradation behaviour is also co-regulated by multiple factors, including doping content, crystalline structure and solubility. This study elucidates the intrinsic relationship among doped elements, structural state and degradation behaviour and provides an experimental support for the precise design and stability regulation of multicomponent functionalised BGNs.

1 | Introduction

Bioactive glass (BG) is a class of inorganic, amorphous nanomaterials characterised by excellent biocompatibility and the unique ability to form bonds with both hard and soft tissues [1, 2]. Over the past decades, significant advances have been made in the synthesis and biological understanding of BG, enabling its widespread clinical application in bone regeneration [3, 4], dental restoration [5], skin repair [6] and cancer therapy [7]. Extensive studies have demonstrated that the degradation of BG in physiological environments releases biologically active ions or ion clusters [8–10], which can trigger specific biochemical responses in vivo, including osteogenic differentiation, angiogenesis, myogenesis, enhanced cell migration and immunomodulation collectively promoting tissue regeneration.

Building on these advances and with the rapid development of nanomaterials technology, bioactive glass nanoparticles (BGNs) have emerged as one of the major focal points in current biomedical materials research and translational applications. Compared with BG prepared by the traditional melt quenching method, BGNs offer several advantages, including controllable particle size, good monodispersity, large specific surface area and superior bioactivity [11–13]. In particular, BGNs prepared via templating strategies exhibit greater flexibility in compositional

tuning, structural design (e.g., mesoporous [6], spherical [8], pinecone-like morphologies [14]) and surface functionalisation. These structural features markedly enhance the biological activities of BGNs in promoting cell migration [15], proliferation [16] and differentiation [16], thereby endowing them with excellent overall performance and broad application prospects in bone tissue regeneration [17], oral rehabilitation [18], drug and gene delivery [19] as well as antitumour therapy and other disease treatment and tissue regeneration clinical scenarios [20, 21].

The sustained bioactivity of BGNs mainly arises from the bioactive ions released from their specific three-dimensional network structure during degradation [22]. Studies have shown that, in physiological environments, BGNs release functional ions via an ion exchange mechanism and thereby trigger a cascade of downstream biological responses [23]. Their overall biological effects are primarily governed by the type, valence state and release kinetics of the doped ions. Under physiologically relevant conditions, BGNs undergo a degradation process dominated by ion exchange and network hydrolysis; firstly, metal ions within the particles first exchange with H^+/H_3O^+ in the surrounding solution, the resulting increase in local pH promotes hydrolysis of the silicate network, the surface Si-OH (silanol) content increases, and this is accompanied by partial silica dissolution and structural rearrangement [24–26]. It is generally accepted that this series of degradation events not only determines the structural stability of the material, but also directly influences the rate and amount of functional ion release, thereby regulating osteogenesis, angiogenesis and immunomodulation over time.

On the other hand, doping with different functional metal elements can not only significantly alter the compactness and chemical stability of the BGN network structure, but also impart distinct biological functions. For example, the introduction of certain transition metal ions can endow the material with antioxidant or antibacterial properties [7, 27], whereas doping with Se or Sr can help enhance osteogenic and anti-inflammatory responses [28, 29]. At the same time, the type, valence state and content of doped elements, by modifying the network structure, further affect the degradation and release kinetics of BGNs and their ability to regulate local pH. Therefore, it is necessary to use binary silicate glass as a base system and conduct systematic comparisons of BGNs doped with different representative metal ions in order to quantitatively elucidate the relationships between composition/structure and degradation behaviour (ion release/pH variation). On this basis, this study employs classical 58S (60 mol% SiO_2, 36 mol% CaO and 4 mol% P_2O_5) as a control group and investigates binary silicate-based BGNs doped with five common functional metal elements (Ca, Mg, Zn, Cu and Mn). By characterising the evolution of particle morphology and size during degradation and combining this with time-dependent analyses of ion release behaviour and changes in solution pH, this work systematically clarifies how different doped elements regulate the degradation characteristics of BGNs, thereby providing fundamental data and theoretical support for the rational design of BGNs targeting specific biological effects.

2 | Materials and Methods

2.1 | Materials

Tetraethyl orthosilicate (TEOS, $C_8H_{20}O_4Si$), triethyl phosphate (TEP, $C_6H_{15}O_4P$), urea (CH_4N_2O) and cetylpyridinium bromide (CPB) were purchased from Sigma-Aldrich. Calcium nitrate tetrahydrate ($Ca(NO_3)_2{\cdot}4H_2O$), magnesium nitrate ($Mg(NO_3)_2$), zinc nitrate hexahydrate ($Zn(NO_3)_2{\cdot}6H_2O$), copper nitrate ($Cu(NO_3)_2$), manganese nitrate tetrahydrate ($Mn(NO_3)_2{\cdot}4H_2O$), cyclohexane, isopropanol, anhydrous ethanol and acetone were obtained from Shaanxi Guoyao Chemical Reagent Co. Ltd.

2.2 | Synthesis of Element-Doped BGNs

Element-doped BGNs were synthesised based on previously reported methods with minor modifications. Briefly, 0.65 mmol CPB and 2.5 mmol urea were dissolved in deionised water under ultrasonication. Subsequently, 7.5 mL of cyclohexane and 0.23 g of isopropanol were added, followed by vigorous stirring at 35°C for 2 h. TEOS was then introduced dropwise, and the temperature was raised to 70°C. After a specific interval, the corresponding metal precursor solution (Ca, Mg, Zn, Cu or Mn nitrate) was added. The reaction proceeded at 70°C for 16 h. After completion, the resulting mixture was washed multiple times with acetone, ethanol and deionised water followed by freeze-drying. The final products were calcined at 600°C/5 h to remove residual organic components.

2.3 | Transmission Electron Microscopy (TEM)

The transmission electron microscope (HT-7800, Hitachi) was used to examine the morphology and microstructure of the BGNs doped with different elements. Specifically, 2 mg of BGN was dispersed in 1 mL of anhydrous ethanol and ultrasonicated for 15 min to obtain a 2 mg/mL suspension. Two drops of this suspension were deposited on a 200-mesh copper grid and air-dried. TEM analysis was then performed under the following conditions: accelerating voltage 100 kV, filament voltage 19.5 V, current 10 mA, vacuum 0.8 Pa, incident electron wavelength 0.037 Å and a specimen-to-film distance of 80 cm.

2.4 | Fourier Transform Infrared Spectroscopy (FTIR)

The structural composition of the BGNs was characterised using a Fourier transform infrared spectrometer (FTIR, Nicolet 6700, Thermo Fisher Scientific). A small amount of sample was evenly spread on the crystal sample holder. The metal probe was then rotated downward until it made full contact with the sample. The spectra were collected over a range of 4000-600 cm^{-1} with 64 scans per sample and a resolution of 4 cm^{-1}.

2.5 | X-Ray Diffraction (XRD)

The chemical composition and crystal structure of BGNs were analysed using an X-ray diffractometer (DMAX-RB, Rigaku). Approximately 10 mg of nanoparticles were evenly spread in the sample holder. The holder was then placed beneath the X-ray source, and measurements were carried out under the

following conditions: operating voltage 40 kV, current 30 mA, scanning range 10°–90° and a scan speed of 5°/min.

2.6 | Energy Dispersive Spectroscopy (EDS)

Elemental semiquantitative analysis of P, Ca, Mg, Zn, Cu and Mn in different BGNs was performed using an energy-dispersive spectrometer (EDS, Oxford X-MaxN) attached to a field-emission scanning electron microscope (SEM, Thermo Fisher Scientific, Quanta 250 FEG).

2.7 | Degradation of Element-Doped BGNs

Equal masses of the different element-doped BGNs were placed in dialysis bags with a molecular weight cut-off of 3500 Da and immersed in 20 mL of 0.9% normal saline to achieve a concentration of 2 mg/mL. The bags were incubated in a shaking incubator at 37°C and 200 rpm. At predetermined time points (3, 7, 14, 28, 45, 60, 90, 120 and 150 days), small amounts of the particles were withdrawn from each bag for TEM observation whereas 10 mL of the external leaching solution was collected for quantitative analysis of ion concentrations using an inductively coupled plasma mass spectrometer (ICP-MS, Agilent 7800, USA); an equal volume of fresh saline was then added to maintain a constant volume. In parallel, 5 mL of the extraction solution from each group was collected at each time point, and the pH was measured using a benchtop pH metre (FiveEasy Plus, Mettler Toledo) to obtain accurate time-dependent profiles of pH variation. Part of the ICP-MS analyses was performed by Scientific Compass (www.shiyanjia.com) in accordance with the standard operating procedures provided on the Scientific Compass.

3 | Results and Discussion

3.1 | Characterisation of BGNs

Monodisperse BGNs doped with different elements were synthesised via a sol-gel method and their morphology was characterised by transmission electron microscopy (TEM). As shown in Figure 1a–f, the classical 58S glass exhibited a spherical, radially branched morphology with an average diameter of approximately 240 nm. In contrast, the binary Ca-doped BGN (BGN-Ca) showed a mesoporous spherical shape with a more loosely packed peripheral structure due to the absence of phosphate stabilisation with a slightly reduced diameter (~280 nm). The Mg-doped BGN (BGN-Mg) presented a morphology similar to BGN-Ca with diameters ranging from 280 to 300 nm. Interestingly, the Zn-doped BGN (BGN-Zn) exhibited a nanoflower-like morphology with a diameter of approximately 320 nm, and similarly, Cu-doped BGN (BGN-Cu) showed a comparable flower-like structure with a diameter of ~320 nm. In contrast, Mn-doped BGN (BGN-Mn) maintained a compact spherical morphology with a diameter of about 200 nm. X-ray diffraction (XRD) was further used to analyse the phase compositions of these binary BGNs. The classical 58S glass displayed a broad amorphous peak centred at $2\theta = 24°$ characteristic of its noncrystalline structure [30](Figure 1g). This amorphous pattern was similarly observed in the other binary BGNs (Figure 1h–j). However, distinctive diffraction peaks were detected in BGN-Cu and BGN-Mn. Specifically, in BGN-Cu, diffraction peaks at $2\theta = 35.5°$, 38.8° and 48.7° corresponded to the (−111), (111) and (−202) planes, respectively, which was consistent with the monoclinic crystal structure of CuO (PDF#48-1548) [31] (Figure 1k). For BGN-Mn, peaks at $2\theta = 32.8°$, 38.12°, 55.08° and 65.67° were indexed to the (222), (400), (440) and (622) planes of Mn_2O_3 (PDF#41-1442) [6] (Figure 1l). It is noteworthy that crystalline CuO and Mn_2O_3 phases were observed only in BGN-Cu and BGN-Mn, respectively, whereas the other BGNs remained amorphous under the same conditions. This difference arises from the fact that, in the binary silicate system, SiO_2 serves as the only network former and all metal oxides act as network modifiers, but the amount that can be stably doped into the amorphous silicate network differs among them. Under a molar feed ratio of 6:4 and a calcination temperature of 600°C, Ca^{2+}, Mg^{2+} and Zn^{2+} can be stably and effectively incorporated into the amorphous silicate network without inducing phase separation. In contrast, Cu^{2+} and Mn^{2+} exhibit lower solubility in the glass matrix and therefore tend to locally accumulate within the mesoporous structure during calcination, subsequently precipitating as CuO and Mn_2O_3 nanocrystals.

Furthermore, Fourier-transform infrared spectroscopy (FTIR) was employed to further investigate the chemical bonding structures of the BGNs (Figure 2a–f). All samples, including 58S and the BGN-Ca, BGN-Mg, BGN-Zn, BGN-Cu and BGN-Mn, exhibited characteristic Si-O-Si stretching vibrations between 1050 and 1100 cm^{-1} and bending vibrations around 800-810 cm^{-1}. A distinct absorption band at 669 cm^{-1} in BGN-Mn was attributed to Mn-O stretching [6, 7, 30]. In contrast, Cu-O vibrations typically appear in the 1000-1200 cm^{-1} range, overlapping with the Si-O-Si signal, making Cu-O bonds unidentifiable in the FTIR spectra. Lastly, elemental composition analysis was performed using energy-dispersive X-ray spectroscopy (EDS) (Figure 2g–l). In the sol-gel synthesised 58S glass, Si and O were the predominant elements, whereas Ca content was relatively low (~0.4%). In BGN-Ca, Ca content further decreased to 0.27% likely due to reduced phosphate levels leading to calcium loss. In other binary BGNs, the relative content of doped metals was as follows: Mg (0.71%), Zn (0.92%), Cu (0.86%), and Mn (3.34%). The notably higher Mn content was attributed to its partial crystallisation into Mn oxide phases, which were deposited within the mesopores and on the surface, forming a nanocrystalline glass structure. It is undeniable that the experimentally measured atomic percentages of the metal elements are all significantly lower than the molar feed ratios, which may result from both the glass synthesis process and the measurement error of EDS. On the one hand, in the sol-gel microemulsion system, a portion of the metal salts that do not participate in the formation of the glass network are removed during the subsequent washing and dispersion steps leading to a final effective doping level far below the theoretical value. On the other hand, EDS is a semiquantitative technique that only reflects the local composition of the particle surface, and the strong Si/O signals further reduce the relative atomic percentages of minor metal elements during normalisation. Therefore, the elemental fraction results presented here are mainly used to confirm the successful incorporation of the metal elements and their trends rather than as an accurate quantitative basis.

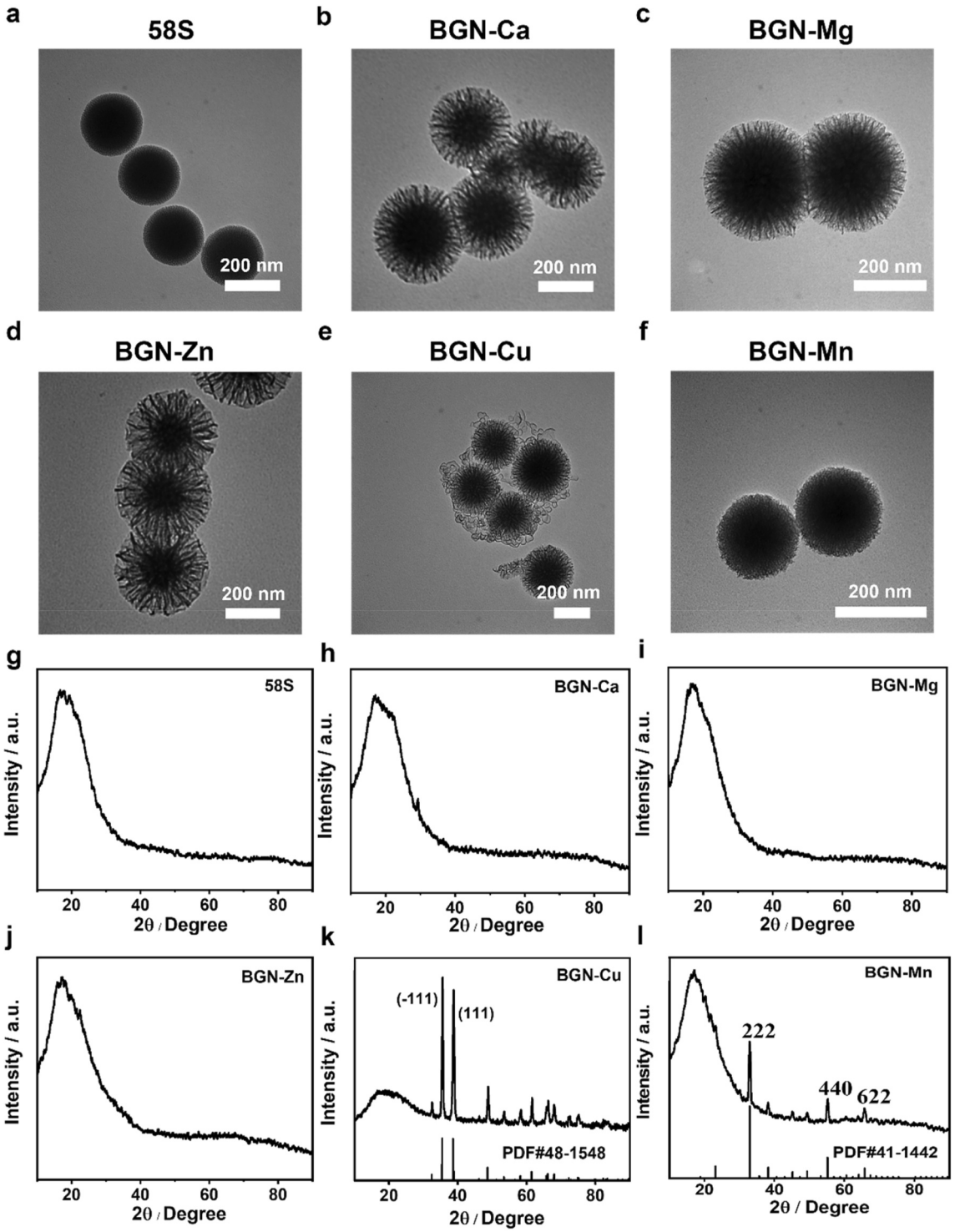

FIGURE 1 | Characterisations of 58S and BGNs doped with different ions. (a–f) TEM images of different BGNs: 58S (a), BGN-Ca (b), BGN-Mg (c), BGN-Zn (d), BGN-Cu (e), BGN-Mn (f). (g–l) XRD patterns of different BGNs: 58S (g), BGN-Ca (h), BGN-Mg (i), BGN-Zn (j), BGN-Cu (k), BGN-Mn (l).

3.2 | Degradation Behaviour of BGNs Observed via TEM

The morphological evolution of BGNs at different time points were monitored by TEM. As shown in Figure 3a–d, the classical 58S glass exhibited slight surface roughness with emerging flocculent structures on day 3, indicating early-stage degradation. In contrast, binary BGN-Ca maintained overall morphological stability, although surface blurring suggested initial dissolution. On day 14, the branched mesopores of 58S became indistinct, and the overall spherical structure appeared more blurred. BGN-Ca exhibited pronounced shrinkage and collapse of the radial mesoporous architecture likely due to calcium ion release accelerating the degradation process. By day 28, the degradation of 58S appeared to plateau maintaining a roughened spherical form. BGN-Ca remained spherical, but its surfaces developed denser, more irregular fibrous clusters with

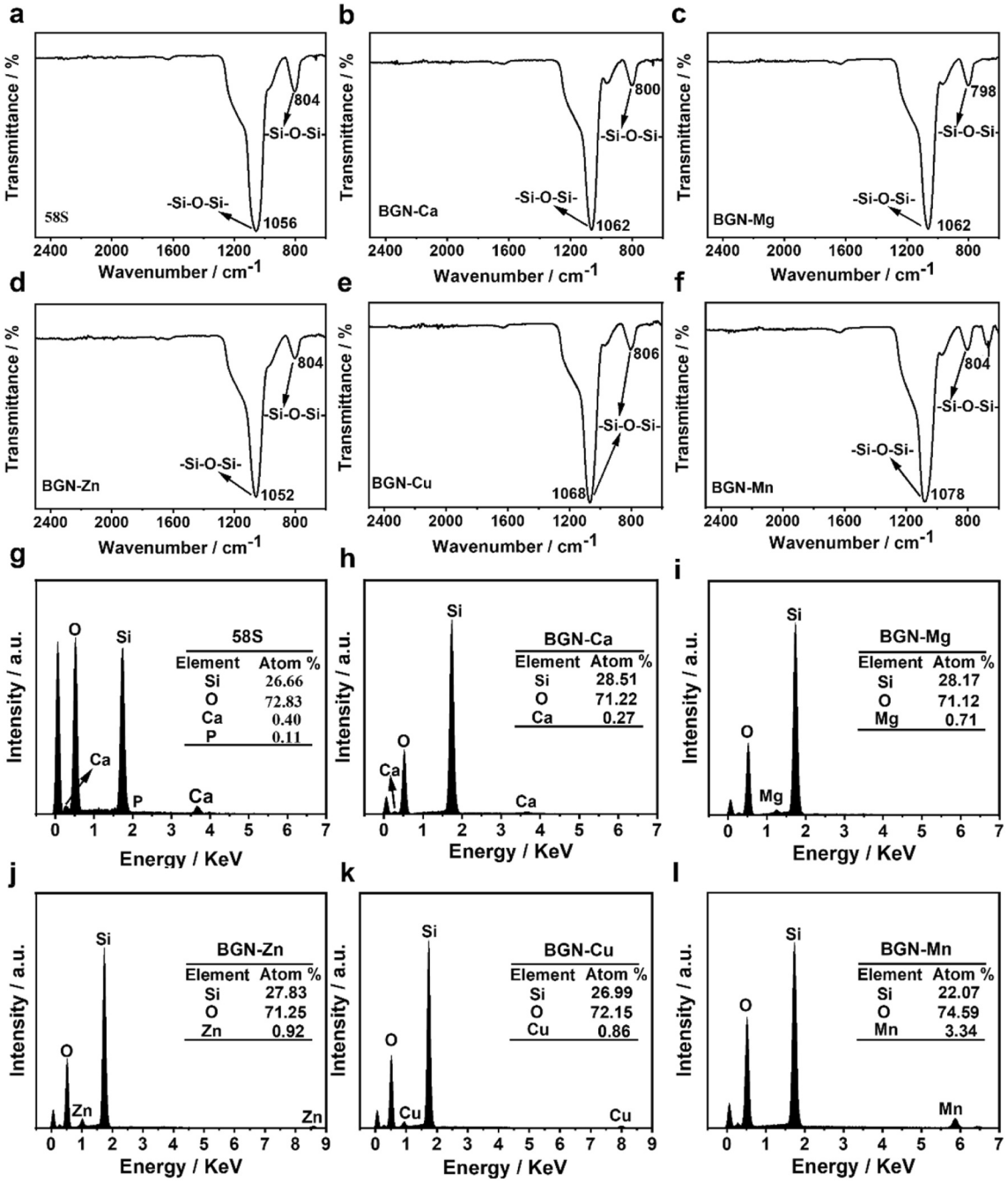

FIGURE 2 | Characterisation of 58S and BGNs doped with different ions. (a–f) FTIR spectra of different BGNs, 58S (a), BGN-Ca (b), BGN-Mg (c), BGN-Zn (d), BGN-Cu (e), BGN-Mn (f). (g–l) EDS spectra analysis of different BGNs, 58S (g), BGN-Ca (h), BGN-Mg (i), BGN-Zn (j), BGN-Cu (k), BGN-Mn (l).

reduced particle diameters. On day 60, the 58S particles further decreased in size and surface smoothness. BGN-Ca underwent a transition from branched mesopores to a rough, broken, and eventually spiked morphology. At day 90, the 58S particles shrank to 120–160 nm and lost their mesoporous structures. BGN-Ca displayed burr-like surfaces and fibre-like degradation features with aggregation and dissolution increasing. At day 120, most BGN particles began to collapse structurally. The size of 58S glass remained similar to day 90. BGN-Ca particles stabilised around 130 nm, but a fraction displayed clustered degradation by-products, suggesting secondary aggregation of degradation residues. By day 150, 58S exhibited obvious surface defects and polygonal contours with loosely connected chain-like structures possibly indicating re-deposition of degradation products or increased interparticle adhesion. Some BGN-Ca particles had collapsed surfaces with blurred edges though a minority retained their spherical framework, suggesting partial preservation of the silica network.

To further compare the effects of different dopants, the morphological evolution of BGN-Mg and BGN-Zn was investigated. As illustrated in Figure 4a–d, on day 3, BGN-Mg retained a stable radial structure with only minimal surface roughening. Notably, the flower-like morphologies of BGN-Zn showed no

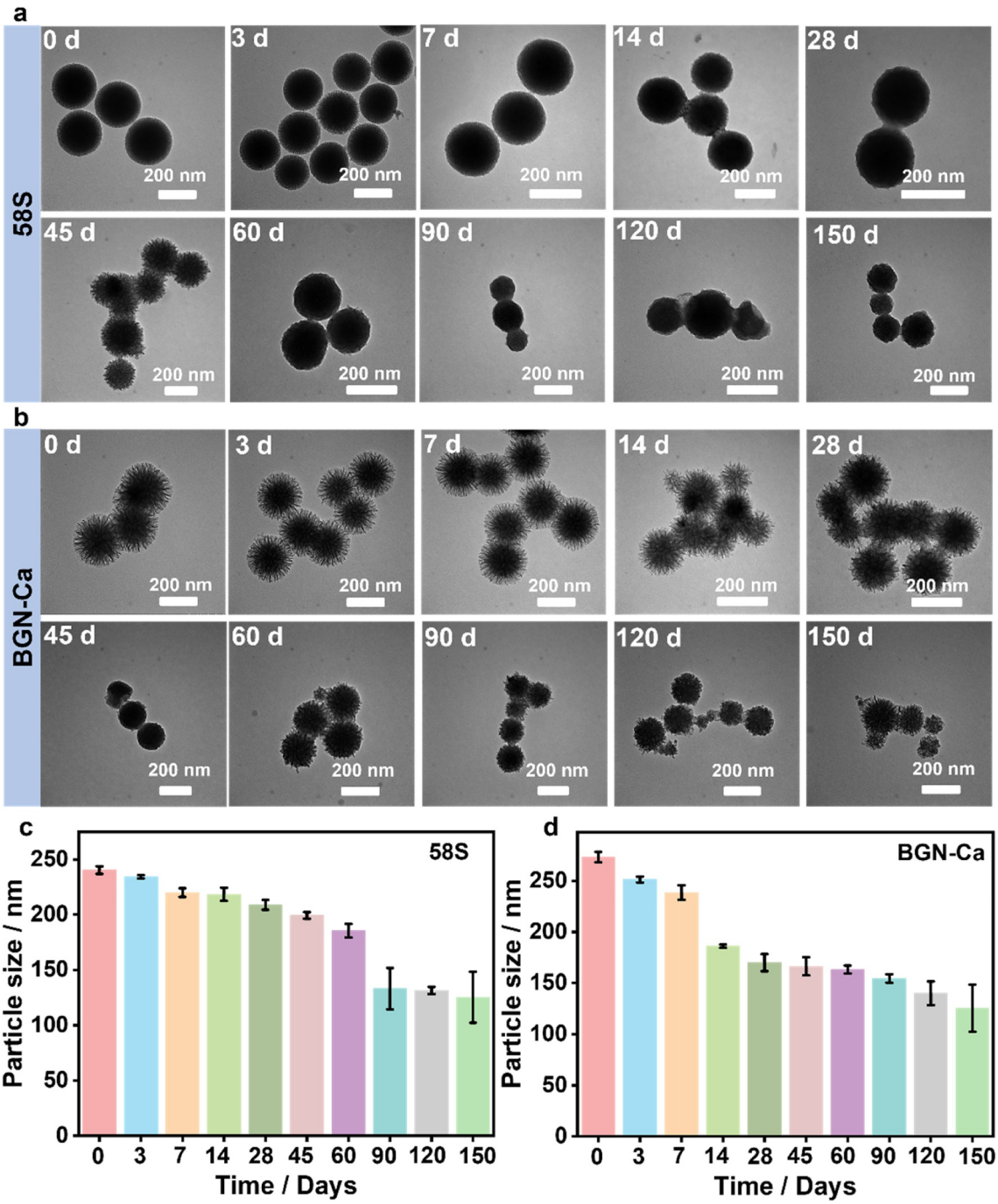

FIGURE 3 | Representative TEM images of the degradation behaviour of 58S and BGN-Ca at different time points, (a) 58S, (b) BGN-Ca. Statistical analysis of particle size variation at different degradation time points, (c) 58S, (d) BGN-Ca.

significant structural alterations at this stage. At day 14, BGN-Mg showed surface loosening and loss of branched structures with emerging fibrous textures. In BGN-Zn, the flower-like particles began disintegrating into irregular, heterogeneous fragments. At day 28, BGN-Mg retained its spherical structure with further reduction in particle size. BGN-Zn exhibited sharp needle-like protrusions, pronounced aggregation and dark degradation by products emerged. On day 60, BGN-Mg experienced collapse of mesoporous frameworks, particle disintegration and increased aggregation. BGN-Zn lost its flower-like morphology entirely with structural damage and aggregation evident; particle size was reduced to 110–150 nm. By day 90, BGN-Zn showed complete loss of nanoflower features with net-like degraded residues surrounding ~140 nm particles. At day 120, BGN-Mg became morphologically irregular with partial loss of native architecture. BGN-Zn exhibited pronounced surface erosion, particle fusion and size variation. BGN-Mg particles (~120 nm) showed signs of aggregation and interconnection on day 150. BGN-Zn structures had fragmented into small clusters with particle fusion and adhesion increasing.

In contrast to BGN-Mg and BGN-Zn, BGN-Cu and BGN-Mn exhibited distinct degradation behaviour. According to Figure 5a–d, on day 3, BGN-Cu and BGN-Mn, as glass-ceramics

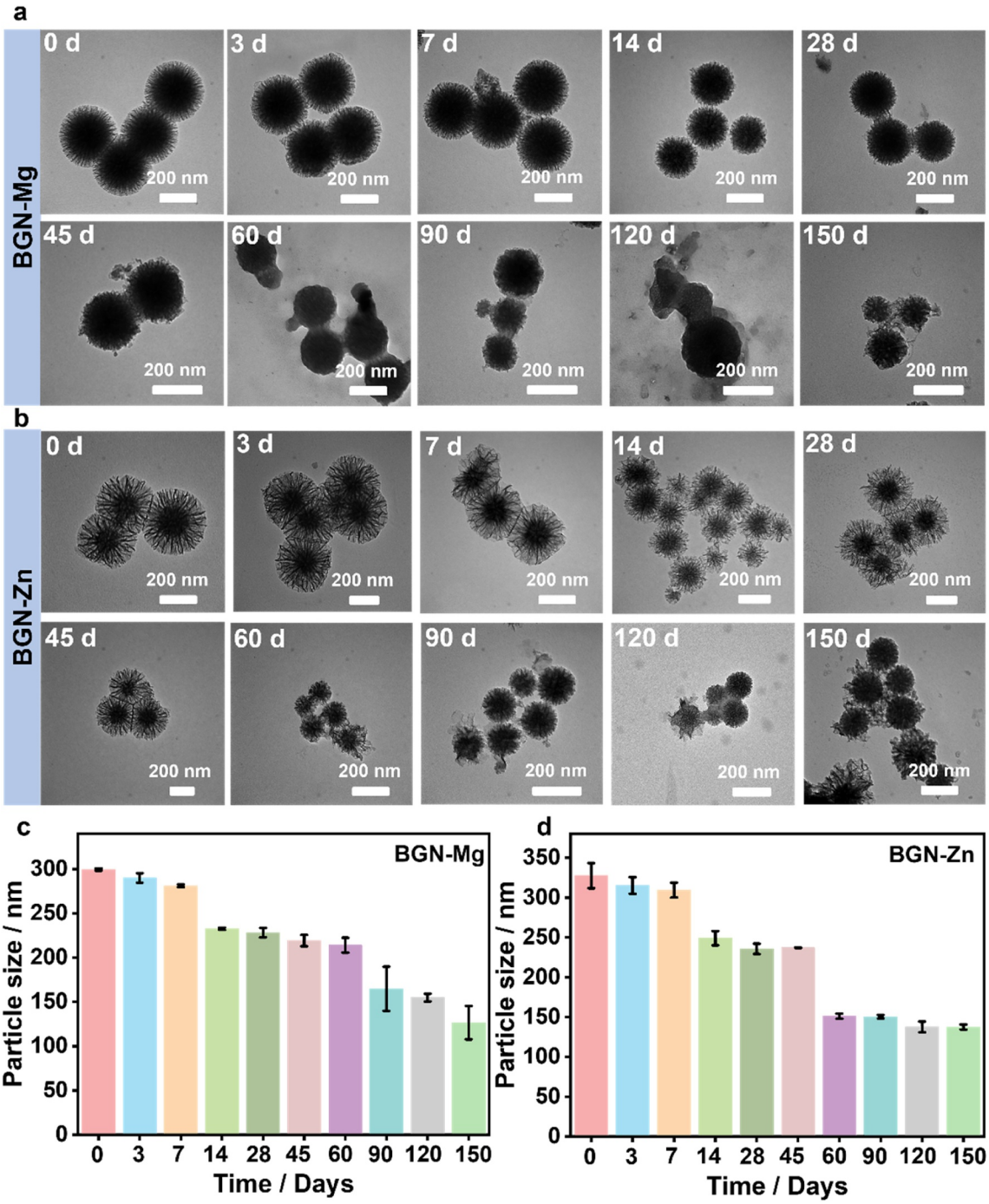

FIGURE 4 | Representative TEM images of the degradation behaviour of BGN-Mg and BGN-Zn at different time points, (a) BGN-Mg, (b) BGN-Zn. Statistical analysis of particle size variation at different degradation time points, (c) BGN-Mg, (d) BGN-Zn.

containing CuO and Mn_2O_3 phases, respectively, showed no notable morphological changes. At day 14, BGN-Cu exhibited the disappearance of its fluffy CuO crystalline domains with the surface becoming more defined and resembling a mesoporous sphere. BGN-Mn underwent a transition from smooth spherical particles bearing flocculent crystallites to irregular aggregates characterised by fibre-like protrusions and roughened surfaces. On day 28, BGN-Cu exhibited further surface softening with blurred mesoporous boundaries. BGN-Mn showed clear particle shrinkage, loss of radial symmetry and roughened surfaces with surrounding degradation products. By day 60, the overall morphology of BGN-Cu remained unchanged, but partial particle fragmentation was observed, accompanied by a sustained size reduction. BGN-Mn exhibited a broad particle size distribution ranging from 90 to 140 nm with pronounced overall degradation. By day 90, BGN-Cu experienced intensified roughness, and the aggregation of CuO crystal was visible. BGN-Mn underwent pronounced disintegration and irregular shaping alongside severe aggregation. By day 150, partial collapse of BGN-Cu occurred and apparently aggregated clusters were formed. BGN-Mn existed mostly as irregular polygonal aggregates with a particle size between 80 and 140 nm.

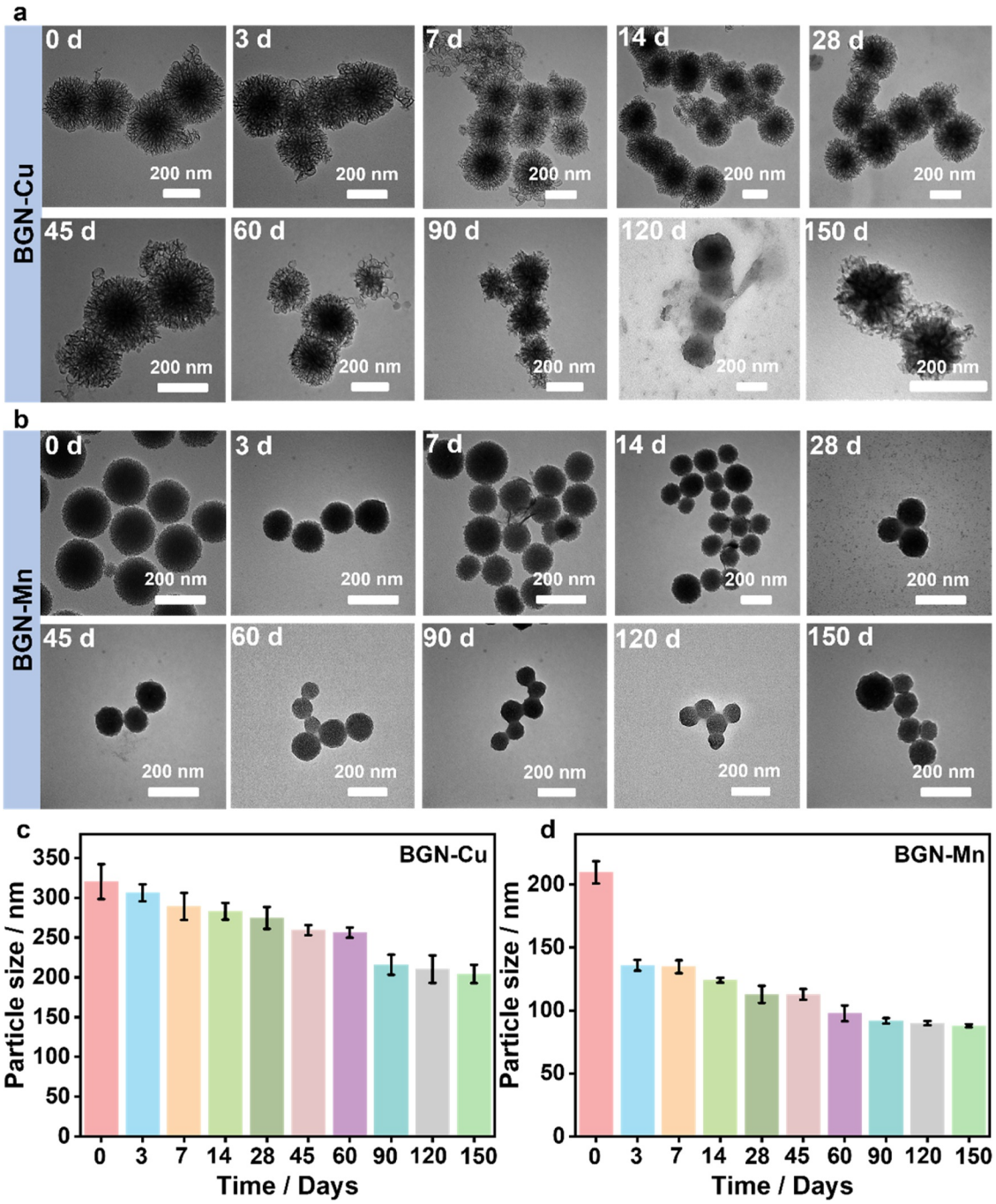

FIGURE 5 | Representative TEM images of BGN-Cu and BGN-Mn degradation behaviour at different time points: (a) BGN-Cu, (b) BGN-Mn. Statistical analysis of particle size variation at different degradation time points, (c) BGN-Cu, (d) BGN-Mn.

In summary, preliminary TEM observations indicated that BGN-Ca and BGN-Mg exhibited the fastest degradation rates, followed by BGN-Mn, BGN-Zn and BGN-Cu. Notably, the classical 58S glass demonstrated enhanced network stability owing to the presence of phosphate groups in its structure and showed the slowest degradation behaviour among all samples, retaining partial spherical frameworks and roughened surfaces even at later stages. These findings suggest that the type of doped metal ion plays a critical role in governing the morphological stability and long-term degradation behaviour of BGNs.

3.3 | Ion Release Kinetics of BGNs

As shown in Figure 6a–i and Supporting Information S1: Figures S1 and S2, the pH variation and ICP-based ion release results further demonstrated that the degradation behaviour of metal-doped BGNs and classical 58S glasses is clearly different particularly in terms of Si and metal ion release profiles. These variations were also closely associated with pH changes during degradation. In terms of Si release kinetics, the concentration of Si in all samples showed a continuous increasing trend, showing a rapid increase within 3 days, followed by a slow release, presenting a typical "fast-then-slow" release pattern.

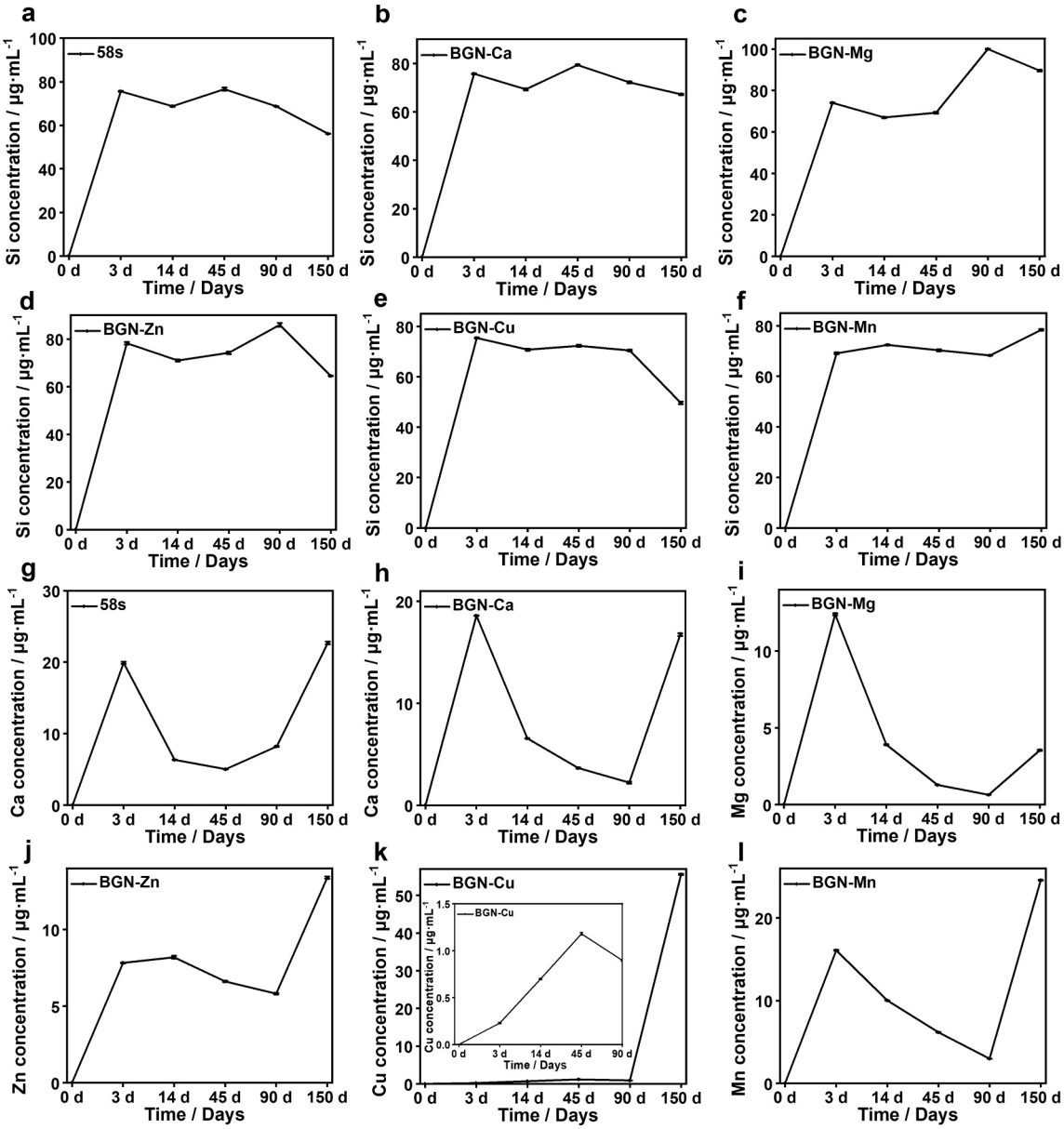

FIGURE 6 | Ion release behaviour of 58S and BGNs doped with different ions. (a–f) Silicon release behaviour of different BGNs: 58S (a), BGN-Ca (b), BGN-Mg (c), BGN-Zn (d), BGN-Cu (e), BGN-Mn (f). (g–l) Release behaviour of metal elements doped into different BGNs: 58S (g), BGN-Ca (h), BGN-Mg (i), BGN-Zn (j), BGN-Cu (k), BGN-Mn (l).

Correspondingly, all groups showed a sharp rise in pH within the initial 3 days, which subsequently transitioned into stable phase. Over the entire degradation period, the total Si release of the BGN-Ca group was slightly higher than that of 58S. This is attributed to the high chemical reactivity of Ca^{2+}, which is readily exchanged with Na^{+} in solution and less prone to precipitation in phosphate-free networks, thereby facilitating its sustained accumulation and release in the solution. Meanwhile, the pH values in the BGN-Ca group generally ranged between 7.2 and 7.8, while those of 58S were maintained around 7.4–7.8. The relatively stable degradation of 58S can be attributed to the presence of P_2O_5, which facilitates the formation of stable Si-O-P and Ca-O-P linkages, thereby strengthening the glass network and contributing to a milder degradation behaviour. Remarkably, the BGN-Mg group exhibited the highest Si release among all samples with a sharp accumulation over the first 90 days and a total release exceeding 90 μg/mL by day 150. This can be ascribed to both the network structure and the high chemical reactivity of Mg. Although both Ca and Mg are chemically active metals, the total Si release from BGN-Ca was lower than that of BGN-Mg, which may be attributed to the significant difference in doping concentration (as indicated by EDS analysis, the Mg content in BGN-Mg was 0.71%, whereas the Ca content in BGN-Ca was only 0.27%). The higher incorporation of Mg^{2+} likely led to increased formation of Si-O-Mg bonds, which disrupted the silicate network more extensively than Si-O-Ca bonds, thereby accelerating glass hydrolysis and enhancing Si release. Notably, the pH in the BGN-Mg group remained stable between 7.0 and 7.8 throughout days 3–120, indicating excellent buffering capacity and degradation control.

The levels of total Si release were comparable between the BGN-Zn and BGN-Mn groups, but the kinetics of release were different. The degradation of BGN-Zn showed a "fast-then-slow" pattern, whereas BGN-Mn exhibited a "slow-then-fast" trend. This disparity is likely related to their structural differences and the crystallinity of BGN-Mn. BGN-Zn remained predominantly amorphous with a relatively loose network that was more susceptible to hydrolysis. As a moderately active metal, Zn^{2+} was easily exchanged and rapidly released in the early phase especially through the cleavage of Si-O-Zn bonds, resulting in fast initial Si release with consequent pH rise. As Zn^{2+} was gradually depleted, the number of reactive sites in the glass decreased leading to a slower Si release rate over time. In contrast, the presence of Mn_2O_3 nanocrystals in BGN-Mn formed a relatively compact microcrystalline structure, which provided physical protection to the surrounding amorphous regions and suppressed early-stage hydrolysis. As a result, Si release was initially limited. However, with progressive degradation, the crystalline phase began to disintegrate exposing previously shielded reactive sites, thus enhancing the Si release rate in the later stages and producing the 'delayed-acceleration' release profile. In the case of BGN-Cu group, rapid hydrolysis of the silicate network occurred during the first 3 days, particularly involving the cleavage of Si-O-Cu bonds, which led to a burst release of Si and a marked increase in OH^- concentration, thereby elevating the pH to approximately 7.6. Due to the relatively low chemical activity of Cu^{2+}, its release remained limited in the early phase resulting in a degradation pattern dominated by a sharp pH rise and rapid Si release. As degradation progressed and hydrolysis slowed, Cu^{2+} ions were gradually released from CuO nanocrystals. The hydrolysis of Cu^{2+} ($Cu^{2+} + H_2O \rightarrow Cu(OH)^+ + H^+$) led to increasing H^+ concentration and progressive acidification of the system [32]. From day 90–150, Cu^{2+} release accelerated significantly, further intensifying acid generation. Compared to other metal ions such as Mg^{2+} and Mn^{2+}, the high concentration of Cu^{2+} catalyse hydrolysis reactions or disrupt the ionic equilibrium in the medium. In addition, the formation of $Cu(OH)^+$ or $Cu(OH)_2$ precipitates further releases H^+ contributing to the acid burden. Collectively, these factors rendered BGN-Cu the most acidifying system among all samples with the sharpest pH decline and the poorest buffering performance during long-term degradation.

To further intuitively compare the overall degradation levels among the different binary BGNs, semiquantitative analyses were performed on the relative release fractions of the doped metal ions and Si at 3 days (Supporting Information S1: Figs. S3 and S4). At 3 days, the release fractions of metal ions in the BGN-Ca, BGN-Mn and BGN-Mg groups were the highest, followed by BGN-Zn, with BGN-Cu the lowest, indicating that the Ca-, Mn- and Mg-doped systems undergo more pronounced early ion exchange and network disruption. Correspondingly, the relative Si release fractions at 3 days showed that the differences among the groups were relatively limited. This suggests that, although different doped ions modify the degradation kinetics and metal release characteristics, the extent of Si network dissolution tends to converge among the groups over long-term scales. Taken together, BGN-Ca, BGN-Mn and BGN-Mg exhibit faster early-stage degradation and ion exchange, BGN-Zn show intermediate behaviour, whereas BGN-Cu display the highest structural stability and the lowest overall degradation degree during long-term immersion.

In summary, the incorporation of different metal elements into BGNs can significantly modulate their structural stability and ion release behaviours. The activity series of metal ions provides a preliminary reference for predicting the early-stage release tendency of BGNs. For instance, highly reactive metals (such as Ca and Mg) tend to undergo rapid ion exchange and controlled release, while maintaining the structural integrity and a mildly alkaline microenvironment, thereby enabling a stable and predictable degradation process. In contrast, moderately reactive metals (such as Zn) generally exhibit more gradual and sustained release behaviours, but their degradation kinetics are often influenced by multiple factors, including dopant-induced network reconstruction, crystallisation and solubility variations. Notably, low reactivity metals (such as Cu) may induce nonlinear degradation behaviours under specific structural conditions. This behaviour is no longer dominated by simple ion exchange mechanisms but rather closely associated with structural instability induced by crystallinity, generation of hydrolytic byproducts (e.g., H^+) and the cleavage of bridging oxygen bonds between metal ions and the silicate network. These complex mechanisms suggest that metal activity alone is insufficient to fully predict the degradation profiles of doped systems. Instead, it must be analysed in conjunction with structural composition and microscopic kinetic features.

It is important to note that the distinct degradation behaviours observed among different BGNs provide important guidance for tailoring their biological functions. In BGN systems, variations in composition and structure induced by different dopant elements can significantly influence degradation behaviour and further regulate ion release kinetics and the dynamic evolution of the local microenvironment, including ion concentration gradients and pH changes. Therefore, elucidating the influence of composition and structural characteristics on degradation behaviour is expected to guide how their biological effects are exerted where they may be best applied, and how long these effects may be sustained.

For example, BGNs exhibiting rapid early-stage degradation and ion release are generally more suitable for applications requiring the rapid establishment of an ionic microenvironment or early-stage regulation, such as wound repair. In contrast, BGNs with slower or stage-dependent degradation profiles are more favourable for maintaining sustained ion supply and long-term microenvironmental regulation, such as in bone tissue regeneration. In this study, the systematic investigation of the long-term degradation behaviours of different metal-doped BGNs not only deepens the understanding of the relationship among elemental properties, structural features and degradation behaviour, but also provides a materials-level basis for the design and selection of BGNs tailored to different disease requirements. It should be noted that the above discussion on biological functions and application suitability is mainly based on degradation characteristics and established knowledge of ion-mediated biological effects. The specific biological responses of different BGNs still require further validation through systematic in vitro and in vivo studies.

Therefore, future studies should consider integrating advanced characterisation and simulation approaches, such as in situ Fourier-transform infrared spectroscopy (FTIR), density functional theory (DFT) simulations and machine learning models, to gain deeper insights into the local coordination environment and dynamic reconstruction processes of doped metal ions in glass matrix [33]. Clarifying the interrelationship among element properties, structural features and functional outcomes will provide a theoretical foundation and experimental guidance for the high-performance design of BGNs with multi-mechanistic therapeutic capabilities, targeted ion therapy and intelligently controllable degradation behaviour in the field of tissue engineering and regenerative medicine.

4 | Conclusion

In this study, a systematic analysis was conducted on the long-term degradation behaviour of binary BGNs. Using classical 58S glass as a control group, five BGN systems doped with different metal elements (Ca, Mg, Zn, Cu and Mn) were constructed. By combining the evolution of particle morphology, ion release behaviour and changes in solution pH, the relationship between doped elements and degradation behaviour was systematically elucidated. The results showed that BGN-Ca and BGN-Mg exhibited the fastest degradation rates, followed by BGN-Zn, BGN-Mn and BGN-Cu. This indicates that although the reactivity of metal ions can, to some extent, predict early ion-exchange processes and initial release trends, the actual degradation behaviour of BGNs is not governed by a single factor but rather is co-regulated by multiple parameters, including doping content, network/crystalline structure, local solubility and microenvironmental feedback. This study reveals the long-term degradation behaviour and ion release characteristics of BGNs doped with different metal elements and provides experimental evidence and theoretical support for the precise design and stability regulation of bioactive glass nanoparticle platforms targeting specific biological effects (such as osteogenesis, angiogenesis, immunomodulation and antibacterial activity).

Acknowledgements

This work was jointly supported by the Natural Science Basic Research Program of Shaanxi of China (Grant 2025JC-YBQN-1078) and Postdoctoral Research Funding Project of Shaanxi of China (Grant 2024BSHSDZZ041).

Funding

This work was jointly supported by the Natural Science Basic Research Program of Shaanxi of China (Grant 2025JC-YBQN-1078) and Postdoctoral Research Funding Project of Shaanxi of China (Grant 2024BSHSDZZ041).

Conflicts of Interest

The authors declare no conflicts of interest.

Data Availability Statement

Data available on request due to privacy/ethical restrictions.

References

1. L. L. Hench, "The Story of Bioglass®," *Journal of Materials Science: Materials in Medicine* 17, no. 11 (2006): 967–978, https://doi.org/10.1007/s10856-006-0432-z.

2. D. E.-S. Ellakwa, A. S. Abu-Khadra, and T. E. Ellakwa, "Insight into Bioactive Glass and Bio-Ceramics Uses: Unveiling Recent Advances for Biomedical Application," *Discover Materials* 5, no. 1 (2025): 78, https://doi.org/10.1007/s43939-025-00254-2.

3. L. Zhou, H. Liu, B. Zhang, et al., "A Novel 3D-Printed Bi-Layer Cranial-Brain Patch Promotes Brain Injury Repair and Bone Tissue Regeneration," *Advanced Functional Materials* 34, no. 18 (2024): 2314330, https://doi.org/10.1002/adfm.202314330.

4. F. Zhao, W. Xie, W. Zhang, et al., "3D Printing Nanoscale Bioactive Glass Scaffolds Enhance Osteoblast Migration and Extramembranous Osteogenesis Through Stimulating Immunomodulation," *Advanced Healthcare Materials* 7, no. 16 (2018): 1800361, https://doi.org/10.1002/adhm.201800361.

5. T. Huang, J. Jia, C. Zhu, et al., "A Novel Mussel-Inspired Desensitizer Based on Radial Mesoporous Bioactive Nanoglass for the Treatment of Dentin Exposure: An *In Vitro* Study," *Journal of the Mechanical Behavior of Biomedical Materials* 152 (2024): 106420, https://doi.org/10.1016/j.jmbbm.2024.106420.

6. J. Tian, Y. Zhao, Q. Zhang, et al., "SOD/CAT-biomimetic Bioactive Glass-Ceramics Nanozyme With Intracellular Oxygen Supply and Immunoregulation for MRSA-Infected Wound Repair," *Chemical Engineering Journal* 513 (2025): 162671, https://doi.org/10.1016/j.cej.2025.162671.

7. W. Niu, M. Chen, Y. Guo, et al., "A Multifunctional Bioactive Glass-Ceramic Nanodrug for Post-Surgical Infection/Cancer Therapy-Tissue Regeneration," *ACS Nano* 15, no. 9 (2021): 14323–14337, https://doi.org/10.1021/acsnano.1c03214.

8. W. Liu, M. Chen, M. Luo, et al., "Bioactive Glass Ions Hydrogels With Antiinflammation Antioxidant Capacity for Treating Inflammation-Related Diseases," *Materials and Design* 227 (2023): 111669, https://doi.org/10.1016/j.matdes.2023.111669.

9. K. Zheng, W. Niu, B. Lei, and A. R. Boccaccini, "Immunomodulatory Bioactive Glasses for Tissue Regeneration," *Acta Biomaterialia* 133 (2021): 168–186, https://doi.org/10.1016/j.actbio.2021.08.023.

10. H. Zhu, K. Zheng, and A. R. Boccaccini, "Multi-Functional Silica-based Mesoporous Materials for Simultaneous Delivery of Biologically Active Ions and Therapeutic Biomolecules," *Acta Biomaterialia* 129 (2021): 1–17, https://doi.org/10.1016/j.actbio.2021.05.007.

11. K. Zheng and A. R. Boccaccini, "Sol-Gel Processing of Bioactive Glass Nanoparticles: A Review," *Advances in Colloid and Interface Science* 249 (2017): 363–373, https://doi.org/10.1016/j.cis.2017.03.008.

12. A. Kumar and C. R. Mariappan, "A Review on Embedding Therapeutic Nanoparticles in Mesoporous Bioactive Glass-Ceramics for Biomedical Applications," *Inorganic Chemistry Communications* 179 (2025): 114855, https://doi.org/10.1016/j.inoche.2025.114855.

13. J. Zhong and D. C. Greenspan, "Processing and Properties of Sol-Gel Bioactive Glasses," *Journal of Biomedical Materials Research* 53, no. 6 (2000): 694–701, https://doi.org/10.1002/1097-4636(2000)53:6<694::aid-jbm12>3.0.co;2-6.

14. F. Kurtuldu, N. Mutlu, M. Michálek, et al., "Cerium and Gallium Containing Mesoporous Bioactive Glass Nanoparticles for Bone Regeneration: Bioactivity, Biocompatibility and Antibacterial Activity," *Materials Science and Engineering: C* 124 (2021): 112050, https://doi.org/10.1016/j.msec.2021.112050.

15. M. Chen, D. D. Winston, M. Wang, et al., "Hierarchically Multifunctional Bioactive Nanoglass for Integrated Tumor/Infection Therapy

and Impaired Wound Repair," *Materials Today* 53 (2022): 27–40, https://doi.org/10.1016/j.mattod.2022.01.019.

16. C. Liu, F. Zhao, W. Zhang, and X. Chen, "Fabrication and Characterization of Novel Rapid-Setting and Anti-Washout Bioactive Glass Cements for Direct Pulp Capping," *Ceramics International* 49, no. 11 (2023): 17827–17837, https://doi.org/10.1016/j.ceramint.2023.02.149.

17. Y. Zhu, X. Zhang, G. Chang, S. Deng, and H. F. Chan, "Bioactive Glass in Tissue Regeneration: Unveiling Recent Advances in Regenerative Strategies and Applications," *Advanced Materials* 37, no. 2 (2025): e2312964, https://doi.org/10.1002/adma.202312964.

18. L. M. Mukundan, S. R. Nirmal, N. Kumar, S. Dhara, and S. Chattopadhyay, "Engineered Nanostructures Within Sol-Gel Bioactive Glass for Enhanced Bioactivity and Modulated Drug Delivery," *Journal of Materials Chemistry B* 10, no. 48 (2022): 10112–10127, https://doi.org/10.1039/D2TB01692C.

19. M. Z. I. Nizami, A. Jindarojanakul, Q. Ma, S. J. Lee, and J. Sun, "Advances in Bioactive Dental Adhesives for Caries Prevention: A State-Of-The-Art Review," *Journal of Functional Biomaterials* 16, no. 11 (2025): 418, https://doi.org/10.3390/jfb16110418.

20. Y. Zhao, W. Qiang, and B. Lei, "Advanced Multifunctional Bioactive Glass Nanoparticles: From Tissue Repair to Theranostics," *Advanced Healthcare Materials* 15, no. 8 (2025): e02192, https://doi.org/10.1002/adhm.202502192.

21. J. R. Jones, "Reprint Of: Review of Bioactive Glass: From Hench to Hybrids," *Acta Biomaterialia* 23 (2015): S53–S82, https://doi.org/10.1016/j.actbio.2015.07.019.

22. D. S. Brauer, "Bioactive Glasses-Structure and Properties," *Angewandte Chemie International Edition* 54, no. 14 (2015): 4160–4181, https://doi.org/10.1002/anie.201405310.

23. N. Saffarian Tousi, M. F. Velten, T. J. Bishop, et al., "Combinatorial Effect of Si^{4+}, Ca^{2+}, and Mg^{2+} Released From Bioactive Glasses on Osteoblast Osteocalcin Expression and Biomineralization," *Materials Science and Engineering: C* 33, no. 5 (2013): 2757–2765, https://doi.org/10.1016/j.msec.2013.02.044.

24. M. M. Pereira and L. L. Hench, "Mechanisms of Hydroxyapatite Formation on Porous gel-silica Substrates," *Journal of Sol-Gel Science and Technology* 7, no. 1–2 (1996): 59–68, https://doi.org/10.1007/BF00401884.

25. A. Hoppe and A. R. Boccaccini, "Biological Impact of Bioactive Glasses and Their Dissolution Products," *Frontiers of Oral Biology* 17 (2015): 22–32, https://doi.org/10.1159/000381690.

26. W. Huang, D. E. Day, K. Kittiratanapiboon, and M. N. Rahaman, "Kinetics and Mechanisms of the Conversion of Silicate (45S5), Borate, and Borosilicate Glasses to Hydroxyapatite in Dilute Phosphate Solutions," *Journal of Materials Science: Materials in Medicine* 17, no. 7 (2006): 583–596, https://doi.org/10.1007/s10856-006-9220-z.

27. M. Lallukka, M. Miola, Z. Najmi, et al., "Cu-doped Bioactive Glass With Enhanced in Vitro Bioactivity and Antibacterial Properties," *Ceramics International* 50, no. 3 (2024): 5091–5103, https://doi.org/10.1016/j.ceramint.2023.11.253.

28. L. Yu, X. Ding, Y. Li, et al., "Sr-incorporated Bioactive Glass Remodels the Immunological Microenvironment by Enhancing the Mitochondrial Function of Macrophages via the PI3K/AKT/mTOR Signaling Pathway," *Bioactive Materials* 6 (2021): 2999–3012, https://doi.org/10.1016/j.bioactmat.2021.02.027.

29. D. Chen, Z. Liang, Z. Su, et al., "Selenium-Doped Mesoporous Bioactive Glass Regulates Macrophage Metabolism and Polarization by Scavenging ROS and Promotes Bone Regeneration *In Vivo*," *ACS Applied Materials and Interfaces* 15, no. 29 (2023): 34378–34396, https://doi.org/10.1021/acsami.3c03446.

30. Y. Wang, M. Luo, T. Li, C. Xie, S. Li, and B. Lei, "Multi-Layer-Structured Bioactive Glass Nanopowder for Multistage-Stimulated Hemostasis and Wound Repair," *Bioactive Materials* 25 (2023): 319–332, https://doi.org/10.1016/j.bioactmat.2023.01.019.

31. K. Varaprasad, M. López, D. Núñez, et al., "Antibiotic Copper Oxide-Curcumin Nanomaterials for Antibacterial Applications," *Journal of Molecular Liquids* 300 (2020): 112353, https://doi.org/10.1016/j.molliq.2019.112353.

32. K. J. Powell, P. L. Brown, R. H. Byrne, et al., "Chemical Speciation of Environmentally Significant Metals With Inorganic Ligands. Part 2: The Cu^{2+}-OH-, Cl-, CO_3^{2-}, SO_4^{2-}, and PO_4^{3-} Systems (IUPAC Technical Report)," *Pure and Applied Chemistry* 79, no. 5 (2007): 895–950, https://doi.org/10.1351/pac200779050895.

33. A. Shearer, A. M. Bossen, B. Kheilnezhad, et al., "Modeling the Structural and Functional Properties of Bioactive Glasses: Atomic to Macro-Scale Perspectives," *Acta Biomaterialia* 202 (2025): 45–65, https://doi.org/10.1016/j.actbio.2025.06.048.

Supporting Information

Additional supporting information can be found online in the Supporting Information section.

Supporting Information S1: bsb270025-sup-0001-suppl-data.docx.